Measurements of cross sections relevant to γ-ray line astronomy

K. T. Lesko, E. B. Norman, R.-M. Larimer, S. Kuhn, D. M. Meekhof,*
S. G. Crane,† and H. G. Bussell‡
Nuclear Science Division, Lawrence Berkeley Laboratory, University of California, Berkeley, California 94720
(Received 28 September 1987)

Gamma-ray production cross sections have been measured for the γ-ray lines which are most strongly excited in the proton bombardments of C, N, O, Mg, Al, Si, and Fe targets of natural isotopic composition. High resolution germanium detectors were used to collect γ-ray spectra at proton bombarding energies of 8.9, 20, 30, 33, 40, and 50 MeV.

INTRODUCTION

Observations of discrete γ-ray lines can provide unique signatures of nuclear reactions occurring in astronomical environments. Because of their highly penetrating nature, γ rays may provide specific information on astrophysical sites which are opaque to longer wavelength radiation. γ-ray lines have been observed within the solar system in solar flare events,[1] and in extra-solar system sites such as the galactic center, Centaurus A, SS-433, and perhaps the Crab Nebula.[2-6] Other astrophysical sites that are expected to produce observable γ-ray lines include supernova remnants and galactic nuclei.[2,3] In addition, when cosmic rays interact with matter in the interstellar medium (ISM), nuclear γ rays can be produced.[2,3]

In principle, discrete line γ-ray spectra can be used to obtain the relative abundances and energy spectra of the particles responsible for the γ-ray production. By studying γ-ray line emission it is hoped to learn about the intensity, spatial distribution, and sources of the low energy component of the cosmic rays. This lower energy component is unobservable within the inner solar system due to the effects of the solar wind on the low energy particles. γ-ray astronomy could also provide information on the composition of the ISM on large scales. Information concerning the composition, grain size, and distribution of interstellar dust grains could also be obtained.[2,3] However, in order to make use of such future spectra, cross sections for the production of nuclear γ rays must be known.

There are several mechanisms which result in γ-ray emission: charged particle induced reactions such as inelastic scattering and spallation reactions, radioactive decay to excited states of nuclei, e^+e^- annihilation, and neutron capture. Within the first category, the high cosmic abundances of hydrogen and helium imply that only proton and α-particle induced reactions need be considered. The surprisingly high velocity of astrophysical particle beams, such as that determined from observations of SS-433 (Ref. 4), has lead us to extend the systematic measurements of γ-ray line production cross sections from proton and α-particle bombardment to higher energies than previously reported.[7-10] We present in this paper results of measurements of γ-ray production cross sections using a proton beam on a variety of targets. In a second work to be published later we will present results for α-particle bombardments. This work is an extension of the earlier measurements of the authors of Refs. 7–9, who determined the γ-ray production cross sections for both proton and α-particle bombardments of a large number of targets from threshold to 23 MeV for proton and from threshold to 27 MeV for α-particle bombardments.

EXPERIMENTAL METHOD

Beams of protons were provided by Lawrence Berkeley Laboratory's 88-Inch Cyclotron over the energy range of 8.9–50 MeV. The beams impinged on targets of C, N, O, Mg, Al, Si, and Fe, all of natural isotopic composition. The target thicknesses varied from 200 μg/cm^2 to 7.56 mg/cm^2 for the various targets. γ rays produced by various reactions were observed by two high purity Ge detectors of 109 cm^3 volume. We used the techniques of Ref. 7 in extracting the angle integrated cross sections. Since the spins and multipolarities of all the transitions we report are low, the angular distributions can be expressed as a sum of the first three even Legendre polynomials. The angle integrated cross section can then be extracted from just two measurements at 30.6° and 109.9° [zeroes of $P_4(\cos\theta)$]. The exception to this was the 6129 keV γ-ray line in ^{16}O, where four terms are needed to express the angular distribution and measurements of at least three angles are required (we made measurements at 26°, 48.8°, 90°, and 104°). In addition, for the bombardment at 33 MeV, angular distributions over a wider range of angles were taken for all targets to confirm the multipolarities of the γ-ray transitions and to serve as a check on our cross section determination techniques. We have neglected the effects of finite beam spot size ($\leq$0.6 cm diameter). We confirmed that the center of rotation for the detectors was the target position using γ-ray sources fixed at the target position. We have also confirmed that the γ-ray attenuation of the scattering chamber was isotropic over the range of angles we investigated. Both of these poten-

tial corrections were found to be insignificant to within the accuracy of this measurement (relative accuracy of 10%). We have neglected the laboratory-to-center-of-mass transformation corrections which largely cancel for the measurements at 30.6° and 109.9°, and are at most 1% for the worst case.

The energy of the beam was varied in ~10 MeV steps from 8.9 to 50 MeV. Data were also collected at 33 MeV, chosen to coincide with the proposed energy per nucleon of matter in the jets SS-433 (Ref. 4). Single parameter energy histograms were collected at each energy and angle combination for all targets with the two detectors. These histograms were stored on magnetic tape for later analysis. The output of a sensitive current integrator was used to trigger a pulser that was fed into both detectors' preamplifiers and into a scaler. This permitted an accurate beam integration and dead-time determination.

In Figs. 1–4, we show typical spectra generated by the bombardment of Mylar, Mg, Si, and Fe targets with 33 MeV protons. The detector was located at 90° to minimize Doppler shifts. The prominent γ rays are labeled on the figures, indicating the decay energy (in keV) and parent nucleus of the decay.

RESULTS

To obtain cross sections from the measurements on the elemental targets, background and deadtime corrected γ-ray yields were determined for the most prominent peaks in each spectrum. These differential cross sections at several angles were then used to obtain relative angle-integrated cross sections using the technique described above. In order to convert our results into absolute cross sections, we normalized our data to those reported in Ref. 7. For those γ-ray lines which could not be normalized to other determinations, we used the measured absolute energy-dependent γ-ray detection efficiency (determined from our measurements and those of Ref. 7) and the measured target thicknesses to calculate the absolute cross sections. The normalizations were performed at $E_{\text{beam}} = 20$ MeV and we used the 8.9 MeV data as a check of our normalization. We did not use the lower energy data as our principal normalization because the cross sections for many of the lines were seen to vary quite rapidly with energy at the lower energies and due to problems in determining our precise beam energy at this energy. Our problem in determining the beam energy was a result of a failure in our NMR system for this single energy and at

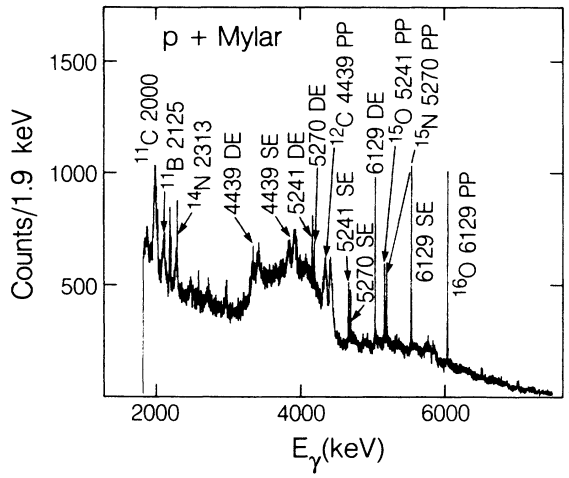

FIG. 1. Typical γ-ray spectra observed for the bombardment of the Mylar target with 33 MeV protons. The γ-ray energy and parent nucleus for the decays are indicated in the figure. The notations PP, SE, and DE represent the photopeak, single escape, and double escape peaks observed within our detectors, corresponding to the detection of the full energy, full energy -511 keV, or full energy -1022 ($=2\times511$) keV, respectively.

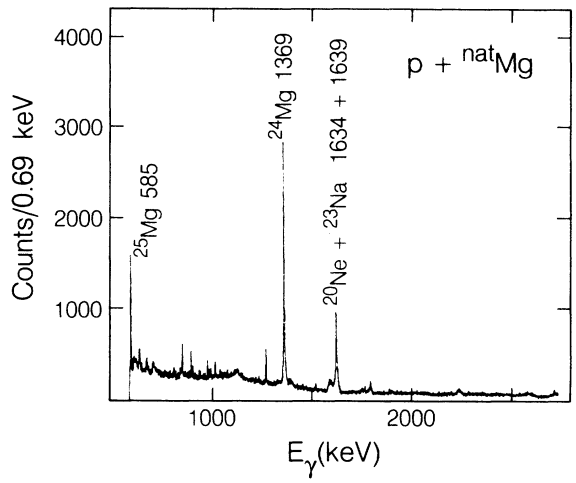

FIG. 2. Typical γ-ray spectra observed for the bombardment of the magnesium target with 33 MeV protons. The γ-ray energy and parent nucleus of the decays are indicated in the figure.

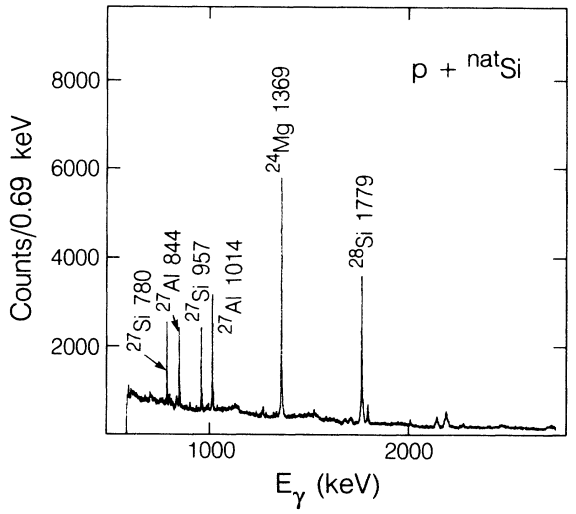

FIG. 3. Typical γ-ray spectra observed for the bombardment of the silicon target with 33 MeV protons. The γ-ray energy and parent nucleus for the decays are indicated in the figure.

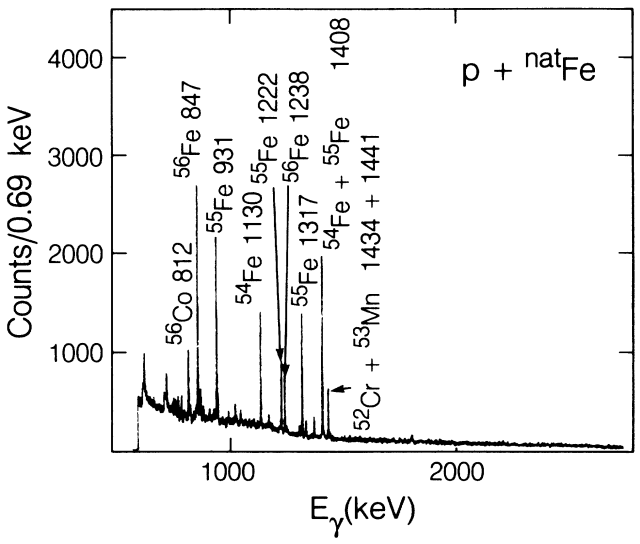

FIG. 4. Typical γ-ray spectra observed for the bombardment of the iron target with 33 MeV protons. The γ-ray energy and parent nucleus for the decays are indicated in the figure.

the higher energies we were able to determine the beam energy accurately (± 5 keV). The cross sections for the 4439 keV line from the Mylar target was normalized at 8.9 MeV due to the significant contributions to this line from other reactions [^{16}O(p,pα)^{12}C*] in the Mylar target at higher energies. We also normalized the 1369 keV line from the Mg target at 8.9 MeV. This was also due to the inclusion of yield to this line from reactions on other isotopes at the higher bombarding energy. We were able to estimate our actual beam energy at the 8.9 MeV bombardment by using our measured γ-ray yields and the 20 MeV normalizations. Using several different targets we were able to determine the energy to be 8.895 ± 0.120 MeV.

Our targets were of natural isotopic composition, whereas those of Ref. 7 were often isotopically enriched. Since our aim was to provide information for γ-ray line astronomy, we felt that natural composition cross sections were more appropriate. In Table I we present the γ-ray lines we have analyzed, listing the principal reactions for their productions, and listing the half-life for radioactive species whose half-lives were short enough to be significant to our data collection times (typically 3–30 min), and the Q values for the different reactions.[11] We have restricted our analysis to include isotopes whose natural abundance is $\geq 1\%$. A number of the γ rays are actually composites of several closely situated lines. Our detector resolution (~ 3 keV at 1 MeV) was such that we did not attempt to resolve these lines. In particular, the line from the Mg target of ~ 1635 keV energy is a composite of the 1633.8 keV line in ^{20}Ne, the 1636.5 keV line in ^{23}Na, and 1611.7 keV line in ^{25}Mg. The 959 keV line from the Si target is a composite of a 960.3 keV transition in ^{29}Al and a 956.8 keV transition in ^{27}Si. The 1435 keV line is a composite of the 1441 keV transition in ^{53}Mn and the 1434 keV transition in ^{52}Cr.

ALL TARGETS

We have attempted to deduce the systematic errors in our data with several checks and several repeat measurements. We estimate the internal consistency of our data to be 10%, while the absolute magnitude can be no more accurate than the data we normalized to, which reported an accuracy of 15% (Ref. 7). With the exceptions noted below, this applies to all our cross sections reported here. We have tabulated our cross section data in Table II.

More complete angular distributions than were required for the cross section extraction were taken for many of the γ-ray lines at 33 MeV bombarding energy. These angular distributions were fitted with the appropriate Legendre polynomials using a least squares fitting routine. Several of these angular distributions and resulting fits are shown in Fig. 5. A comparison of the angle integrated cross sections for these lines obtained with the more complete angular distributions (using the fitted Legendre polynomials) to the abbreviated distributions (using the techniques described above) were found to agree to within the statistical errors of the measurements.

CARBON TARGET

The carbon target was a self-supporting 991 μg/cm^2 thick foil of natural isotopic composition. The yield of

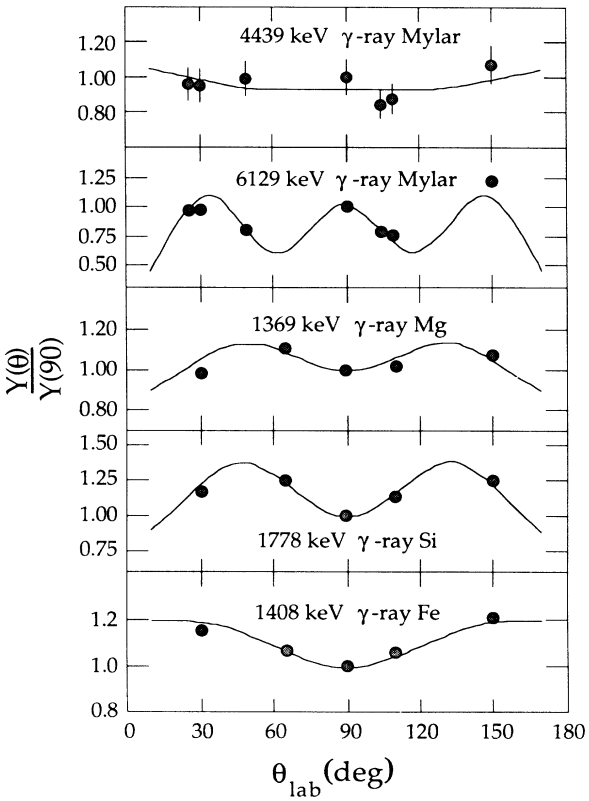

FIG. 5. Angular distributions for five separate γ-ray transitions resulting from the bombardment of Mylar, Mg, Si, and Fe targets with 33 MeV protons. The solid lines are the results of least squares fits of Legendre polynomials to the data.

4439 keV γ rays from the decay of the first excited state to the ground state in ^{12}C is shown in Fig. 6 along with the data of Refs. 7 and 12. The 4439 keV γ ray presents a challenge to correctly extract and integrate. The decaying state responsible for the line is very short lived,[11] and subsequently the γ-ray line is quite broad and Doppler shifted. The Compton scattering of the γ ray in the Ge crystal results in a rapidly rising background below the photopeak. This is illustrated in Fig. 1. We have extracted the photopeak, single, and double escape peaks, but due to the problems in establishing background estimates for the escape peaks, these were used primarily as checks on our consistency of our peak extractions. We established the peak area by setting a broad window on the

TABLE I. Reactions which are responsible for the various γ-ray lines in the present work. The half-life for the radioactive species which significantly contributed to the yields and the Q values for forming the decaying states are listed. Multiple γ rays which were not resolvable in our detector are indicated.

Target	Reaction	E_γ (keV)	$t_{1/2}$	Q (MeV)
C	$^{12}C(p,p')^{12}C$	4443		−4.443
	$^{13}C(p,d)^{12}C$	4443		−7.165
	$^{12}C(p,n)^{12}N$	4443	11.0 ms	− 18.120
	$^{13}C(p,2p)^{12}N$	4443	11.0 ms	−21.502
N	$^{14}N(p,p')^{14}N$	1634.9		−3.948
	$^{14}N(p,n)^{14}O$	1634.9	70.6 s	−5.923
N	$^{14}N(p,p')^{14}N$	2312.9		−2.313
	$^{14}N(p,n)^{14}O$	2312.9	70.6 s	−5.923
O	$^{16}O(p,p\alpha)^{12}C$	4443		−11.605
	$^{16}O(p,n\alpha)^{12}N$	4443	11.0 ms	−25.282
O	$^{16}O(p,d)^{15}O$	5241		−17.398
O	$^{16}O(p,2p)^{15}N$	5270		−18.679
O	$^{16}O(p,p')^{16}O$	6129		−6.129
Mg	$^{24}Mg(p,p')^{24}Mg$	1368.59		−1.369
	$^{25}Mg(p,d)^{24}Mg$	1368.59		−6.476
	$^{26}Mg(p,t)^{24}Mg$	1368.59		−11.311
	$^{24}Mg(p,n)^{24}Al$	1368.59	7.18 s	−14.661
	$^{25}Mg(p,2n)^{24}Al$	1368.59	7.18 s	−21.992
	$^{26}Mg(p,3n)^{24}Al$	1368.59	7.18 s	−33.084
Mg	$^{25}Mg(p,p')^{25}Mg$	1611.7		−1.6117
	$^{26}Mg(p,d)^{25}Mg$	1611.7		−10.480
	$^{26}Mg(p,\alpha)^{23}Na$	1636.5		−3.894
	$^{24}Mg(p,p\alpha)^{20}Ne$	1633.8		−10.947
	$^{24}Mg(p,2p)^{23}Na$	1636.5		−13.766
	$^{25}Mg(p,^3He)^{23}Na$	1636.5		−14.119
	$^{25}Mg(p,d\alpha)^{20}Ne$	1633.8		−15.370
	$^{26}Mg(p,^7Li)^{20}Ne$	1633.8		−18.422
	$^{24}Mg(p,n\alpha)^{20}Na$	1633.8	0.446 s	−23.982
	$^{25}Mg(p,2n\alpha)^{20}Na$	1633.8	0.446 s	−31.083
	$^{26}Mg(p,3n\alpha)^{20}Na$	1633.8	0.446 s	−41.878
Al	$^{26}Al(p,d)Al^{26m}$	829		−12.119
Al	$^{27}Al(p,p')^{27}Al$	843.76		−0.844
Al	$^{27}Al(p,p')^{27}Al$	1014.46		−1.104
	$^{27}Al(p,n)^{27}Si$	1014.46	4.1 s	−5.591
Al	$^{27}Al(p,2p)^{26}Mg$	1129.7		−8.530
Al	$^{27}Al(p,\alpha)^{24}Mg$	1368.59		−1.601
	$^{27}Al(p,tn)^{24}Al$	1368.59	2.07 s	−35.773
Al	$^{27}Al(p,2p)^{26}Mg$	1808.7		−8.271
Si	$^{28}Si(p,d)^{27}Si$	780.3		−15.733
	$^{29}Si(p,t)^{27}Si$	780.3		−17.950
	$^{30}Si(p,tn)^{27}Si$	780.3		−28.559
Si	$^{30}Si(p,\alpha)^{27}Al$	843.76		−3.2863
	$^{28}Si(p,2p)^{27}Al$	843.76		−12.430
	$^{29}Si(p,^3He)^{27}Al$	843.76		−13.186
Si	$^{28}Si(p,d)^{27}Si$	956.8		−15.912
	$^{30}Si(p,2p)^{29}Al$	960.3		−16.693
	$^{29}Si(p,t)^{27}Si$	956.8		−18.129
	$^{30}Si(p,tn)^{27}Si$	956.8		−28.738
Si	$^{30}Si(p,\alpha)^{27}Al$	1014.46		−3.388
	$^{28}Si(p,2p)^{27}Al$	1014.46		−12.600
	$^{29}Si(p,^3He)^{27}Al$	1014.46		−13.356
	$^{28}Si(p,d)^{27}Si$	1014.46	4.13 s	−15.733
	$^{29}Si(p,t)^{27}Si$	1014.46	4.13 s	−17.950
	$^{30}Si(p,tn)^{27}Si$	1014.46	4.13 s	−28.559
Si	$^{28}Si(p,p\alpha)^{24}Mg$	1368.59		−11.353
	$^{29}Si(p,d\alpha)^{24}Mg$	1368.59		−17.603
	$^{30}Si(p,^7Li)^{24}Mg$	1368.59		−21.955
	$^{28}Si(p,n\alpha)^{24}Al$	1368.59	7.18 s	−24.646
	$^{29}Si(p,2n\alpha)^{24}Al$	1368.59	7.18 s	−33.120
	$^{30}Si(p,3n\alpha)^{4}Al$	1368.59	7.18 s	−43.729
Si	$^{28}Si(p,p')^{28}Si$	1778.9		−1.779
	$^{29}Si(p,d)^{28}Si$	1778.9		−8.029
	$^{30}Si(p,t)^{28}Si$	1778.9		−12.380
	$^{28}Si(p,n)^{28}P$	1778.9	0.270 s	−15.113
	$^{29}Si(p,2n)^{28}P$	1778.9	0.270 s	−23.587
	$^{30}Si(p,3n)^{28}P$	1778.9	0.270 s	−32.567
Fe	$^{56}Fe(p,p')^{56}Fe$	846.8		−0.847
	$^{57}Fe(p,d)^{56}Fe$	846.8		−6.269
Fe	$^{56}Fe(p,d)^{55}Fe$	931.4		−9.903
	$^{57}Fe(p,t)^{55}Fe$	931.4		−11.292
Fe	$^{54}Fe(p,p')^{54}Fe$	1129		−2.539
	$^{54}Fe(p,n)Co^{54m}$	1129	1.46 min	−9.222
	$^{56}Fe(p,t)^{54}Fe$	1129		−14.552
	$^{57}Fe(p,tn)^{54}Fe$	1129		−28.455
	$^{56}Fe(p,3n)Co^{54m}$	1129	1.46 min	−29.720
	$^{57}Fe(p,4n)Co^{54m}$	1129	1.46 min	−37.363
Fe	$^{56}Fe(p,d)^{55}Fe$	1222		−11.511
	$^{57}Fe(p,t)^{55}Fe$	1222		−12.900
Fe	$^{56}Fe(p,p')^{56}Fe$	1238		−2.085
	$^{57}Fe(p,d)^{56}Fe$	1238		−7.507
Fe	$^{56}Fe(p,d)^{55}Fe$	1316.7		−10.289
	$^{57}Fe(p,t)^{55}Fe$	1316.7		−11.678
Fe	$^{54}Fe(p,p')^{54}Fe$	1408.4		−1.408
	$^{54}Fe(p,n)Co^{54m}$	1408.4	1.43 min	−9.222
	$^{56}Fe(p,d)^{55}Fe$	1408.5		−10.381
	$^{57}Fe(p,t)^{55}Fe$	1408.5		−11.770
	$^{56}Fe(p,t)^{54}Fe$	1408.4		−13.422
	$^{57}Fe(p,tn)^{54}Fe$	1408.4		−23.967
	$^{56}Fe(p,3n)Co^{54m}$	1408.4	1.43 min	−29.720
	$^{57}Fe(p,4n)Co^{54m}$	1408.4	1.43 min	−37.363
Fe	$^{56}Fe(p,\alpha)^{53}Mn$	1441		−1.627
	$^{56}Fe(p,p\alpha)^{52}Cr$	1434.08		−9.048
	$^{57}Fe(p,n\alpha)^{53}Mn$	1441		−9.273
	$^{54}Fe(p,2p)^{53}Mn$	1441		−9.427
	$^{47}Fe(p,^6Li)^{52}Cr$	1434.08		−12.996
	$^{54}Fe(p,3p)^{52}Cr$	1434.08		−16.848

TABLE II. The six energies investigated, the γ-ray energies, target and daughter nuclei, and our measured cross sections. The γ-ray energies are listed in keV, beam energies in MeV, and the cross sections are in mb. Where we were able to normalize to Ref. 7, our errors are 15%, for those systems where we needed to calculate the absolute γ-ray detection efficiency in order to deduce the absolute cross sections, the errors are 17% (see text). The accuracy of the relative measurement within any excitation function is 10%.

γ energy	4438[a]	1635[b]	2315[b]	6129[b]	4438[a]	5270[a]	5241[a]	1369[b]	1635[a]	829[a]	844[a]	1014[a]	1130[a]	1369[a]	1809[a]
Target	C	N	N	O	O	O	O	Mg	Mg	Al	Al	Al	Al	Al	Al
Residual Nuclei	^{12}C	^{14}N ^{14}O	^{14}N ^{14}O	^{16}O	^{12}C	^{15}N	^{15}O	^{24}Mg ^{24}Al	^{20}Ne ^{20,23}Na	Al^{26m}	Al^{27}	Al^{26m} ^{27}Si	^{26}Mg	^{24}Mg ^{24}Al	^{26}Mg
Beam Energy															
8.895	470.9	61.3	82.0	69.0	c	c	c	516.0	22.0	c	44.1	89.4	3.07	76.5	
20.0	126.1	12.3	24.8	93.9	138.8			357.9	133.0	24.6	18.7	50.5	24.5	29.4	102.3
30.0	79.3	6.26	11.9	55.9	98.8	14.9	24.1	243.5	152.1	45.7	19.8	59.8	26.9	14.8	83.9
33.0	78.4	8.36	10.1	47.1	84.6	13.2	27.8	215.9	131.2	40.0	23.1	53.7	22.1	15.7	76.3
40.0	51.7	5.20	6.72	30.0	70.1	7.78	16.2	186.2	81.4	33.2	23.0	45.6	18.7	42.1	67.1
50.0	22.6			26.6	20.0			124.4	53.5	35.5	29.8	47.7		78.4	61.3
γ energy	780[a]	844[a]	959[a]	1014[a]	1369[a]	1778[b]	847[b]	931[b]	1129[a]	1222[a]	1238[b]	1317[b]	1408	1435[a]	
Target	Si	Si	Si	Si	Si	Si	Fe	Fe	Fe	Fe	Fe	Fe	Fe	Fe	
Residual Nuclei		^{27}Si	^{27}Al ^{29}Al	^{27}Si ^{27}Si	^{27}Al ^{24}Al	^{24}Mg ^{28}P	^{28}Si	^{56}Fe	^{55}Fe Co^{54m}	^{54}Fe	^{55}Fe	^{56}Fe	^{55}Fe Co^{54m}	^{54,55}Fe ^{53}Mn,^{52}Cr	
Beam Energy															
8.895	c	0.94	c	1.47	c	307.8	321.2	c	6.69	c	81.7	c	29.0	2.83	
20.0	2.67	17.1	0.62	4.02	49.0	212.3	242.6	206.0	10.4	47.4	109.4	150.9	59.8	30.4	
30.0	12.1	20.6	17.3	35.0	99.0	114.6	180.8	199.3	40.4	99.9	59.0	178.7	150.6	65.0	
33.0	13.7	20.3	18.7	30.0	90.4	102.9	199.0	155.7	85.4	75.9	58.6	138.4	221.6	64.9	
40.0	12.5	21.6	13.6	28.7	51.1	83.0	182.2	109.7	173.7	39.2	49.8	68.5	271.6	37.6	
50.0					30.0	59.5	202.0	118.2	215.4		43.5	49.2	229.8		

[a]17% absolute error.
[b]15% absolute error.
[c]Below threshold for reaction.

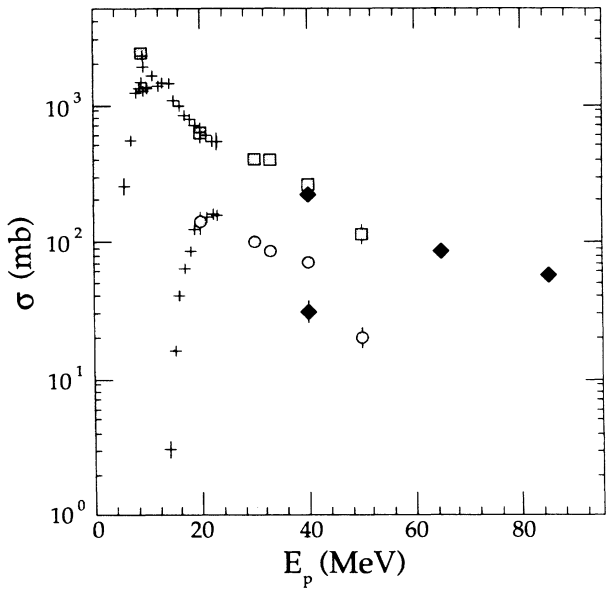

FIG. 6. γ-ray production cross sections for the production of the 4439 keV line from carbon and oxygen targets are indicated by the shaded boxes and shaded circles, respectively. In this and subsequent figures the data of Ref. 7 are plotted as small crosses and those of Ref. 12 are presented as solid diamonds. The data from the carbon target have been multiplied by a factor of 5. Representative errors are indicated on a number of data points for this and subsequent figures.

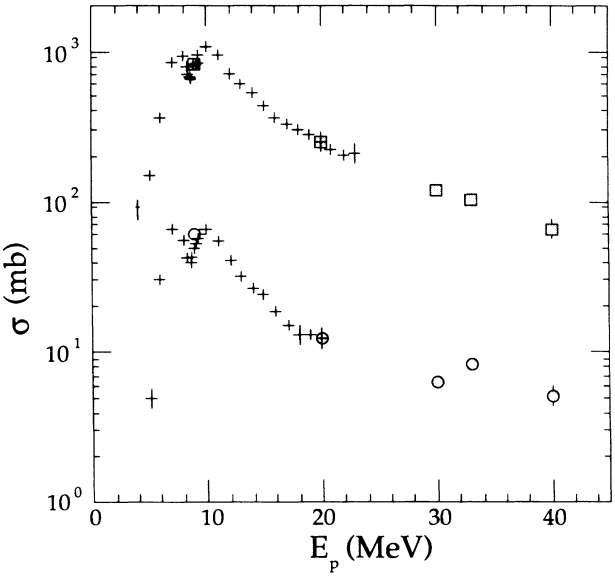

FIG. 7. γ-ray production cross sections for the production of 1635 (shaded circles) and 2315 (shaded boxes) keV lines from the nitrogen target. The data for the 2315 keV line have been multiplied by a factor of 10.

photopeak and a window just above the peak. We assumed that the background was essentially flat surrounding the peak, and that the sharp rise witnessed just below the 4439 keV line is due to Compton scattering in the detector. We have enlarged our errors for the extraction of the 4439 keV line to 17%.

NITROGEN TARGET

The nitrogen target was 1.9 mg/cm^2 of melamine ($N_6C_3H_6$) deposited on a 98 μg/cm^2 natural carbon foil. The 1635 and 2315 lines produced in the decay of the second excited state to the first excited state and the decay of the first excited state to the ground state of ^{14}N, respectively, were extracted and integrated. The excitation functions for these lines are shown in Fig. 7 along with the data of Ref. 7.

OXYGEN TARGET

The oxygen target was a thin Mylar foil (3.3 mg/cm^2, $C_5H_4O_2$). We report the cross section for the inelastic scattering to the second excited state in ^{16}O which results in a 6129.2 keV γ ray. For this target we collected data at the four angles as prescribed by the techniques described above to extract the angle integrated cross sections. We have extracted the photopeak, single escape, and double escape peaks as a consistency check. We ultimately normalized all three excitation functions to the data of Ref. 7, averaging the three separate peak extractions. In Fig. 8 we present our excitation function, along with the data of Ref. 7 at the lower energies, and the data of Refs. 12 and 13 at the higher energies.

The 5270 keV line results from the decay of the first excited state of ^{15}N formed by the ^{16}O(p,2p)^{15}N reaction. The Q value is sufficiently high that in their experiment Dyer *et al.* were unable to observe this line except at their highest energies. In order to obtain the normaliza-

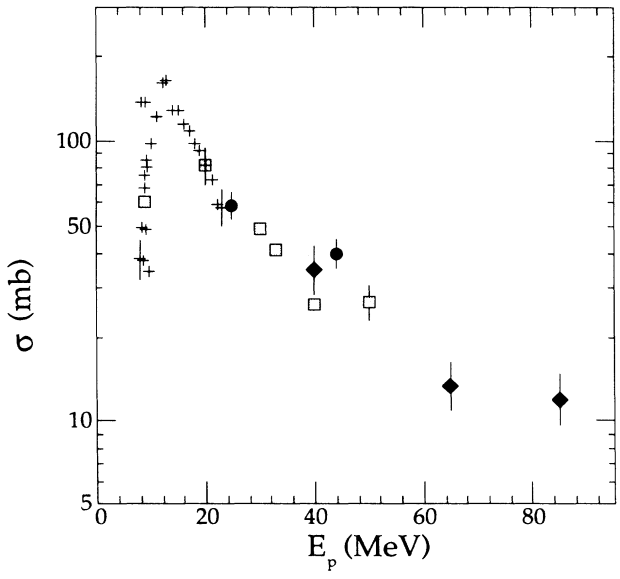

FIG. 8. γ-ray production cross sections for the production of the 6129 keV line from oxygen target (shaded boxes). In addition to the data of Refs. 7 and 12, those of Ref. 13 are shown with solid circles.

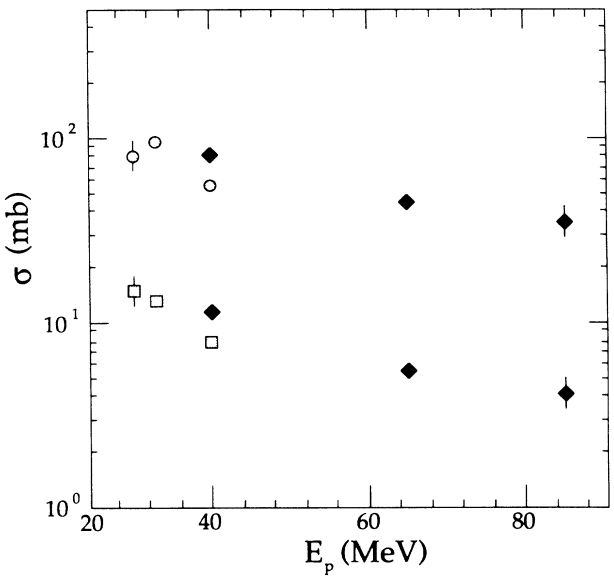

FIG. 9. γ-ray production cross sections for the production of the 5241 (shaded circles) and 5270 (shaded boxes) keV lines from the oxygen target. The data for the 5241 keV line have been increased by a factor of 5.

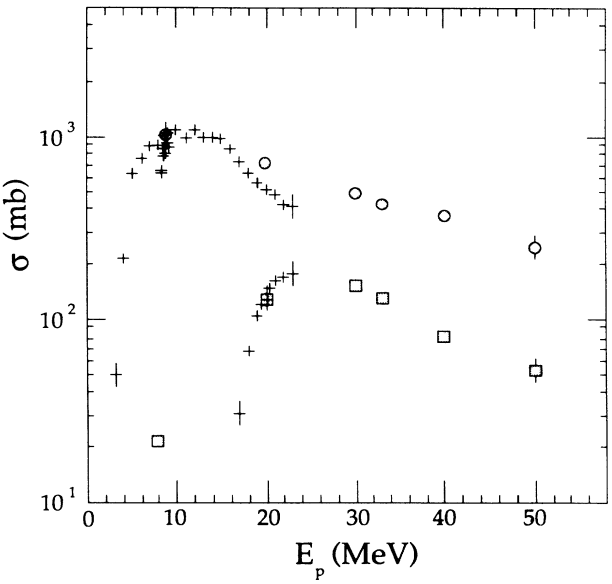

FIG. 10. γ-ray production cross sections for the production of the 1369 (shaded circles) and 1635 (shaded boxes) keV lines from the magnesium target. The data for the 1369 keV line have been increased by a factor of 2. The discrepancy between our data and those of Ref. 7 at 20 MeV for the 1369 keV line is explained by the additional isotopes in our target which contributed to the yield at 20 MeV, where as Dyer *et al.* used an isotopically enriched target.

tion factors for this cross section, we interpolated the absolute detection efficiency for our detectors from the normalizations obtained for the 4439 and 6128 keV lines. Because of the increased uncertainty introduced by this technique we increase our estimate of the error for this line to 17%. Similarly, the 5240 keV line from decay of the second excited state to the ground state in ^{15}O was observed. These excitation functions are shown in Fig. 9, along with the data of Ref. 12.

From the oxygen target we also extracted cross sections for the production of the 4439 keV γ ray. By comparing the yield of 4439 keV γ rays from the Mylar and carbon targets at 8.9 MeV bombarding energy, where other reactions are forbidden by energy considerations, we can obtain the necessary normalizations to subtract the inelastic yield from the carbon component of the Mylar target. The discussion included above concerning the extraction of the 4439 MeV γ ray from the carbon target also applies to this target. The final uncertainty for our cross sections shown in Fig. 6 for the 4439 keV line is 17%.

MAGNESIUM TARGET

The 1369 and 1635 keV lines were obtained from a 2.55 mg/cm^2 thick foil of natural isotopic composition. The 1369 keV line resulted from the decay of the first excited state of ^{24}Mg to the ground state, while the 1635 keV is the composite of three lines: one from the decay of the second to the first excited states in ^{23}Na (1636.5 keV), the second from the decay of the first excited state to the ground state in ^{20}Ne (1633.8 keV), and the third is the decay of the third excited state to the ground state in ^{25}Mg (1611.7 keV). The short lifetime of this last state produced a strongly Doppler shifted and broad line which could not be separated from the two higher energy lines. The 1369 keV excitation function was normalized to Ref. 7. The 1635 keV excitation function was normalized using the extrapolated absolute γ-ray detection efficiency determined from the 1369 keV cross sections and the target thickness. The disagreement between our measurement and that of Ref. 7 at 8.9 MeV is due to the inclusion of the other isotopes in our target which account for substantial yield at lower energies. Notably the 1611 keV γ ray's excitation function persists at much lower energies. The agreement at 20 MeV is fortuitous. These excitation functions are presented in Fig. 10.

ALUMINUM TARGET

Six lines formed by several different reactions were observed using a 6.75 mg/cm^2 natural aluminum foil. The 829 keV line resulted from the decay of the third excited state to the first excited state in ^{26}Al. The 844 and 1014 keV lines were produced in the decay of the first and second excited states to the ground state of ^{27}Al. The 1130 and 1809 keV lines result from the decay of the second excited state to the first, and the decay of the first excited state to the ground state in ^{26}Mg. The 1369 keV line was produced in the decay of the first excited state of ^{24}Mg. The absolute cross sections were obtained by interpolating the detection efficiency for these energies from the iron target and the measured target thicknesses. Uncertainties in the target thicknesses and the detection efficiency increase the reported uncertainties in our abso-

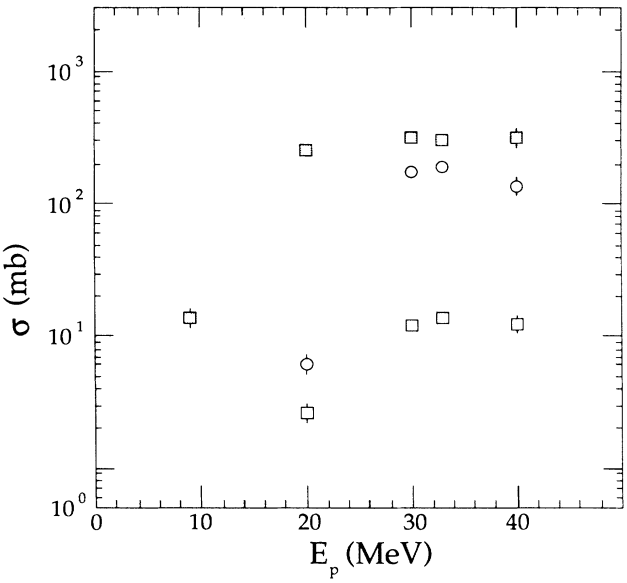

FIG. 11. γ-ray production cross sections for the production of the 780 (open boxes), 844 (shaded boxes), and 959 (open circles) keV lines from the silicon target. The data for the 844 (959) keV line have been increased by a factor of 15 (10), respectively.

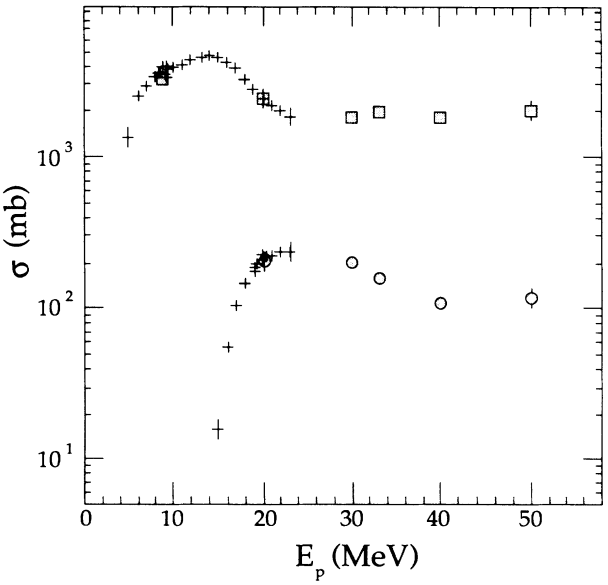

FIG. 13. γ-ray production cross sections for the production of the 847 (shaded boxes) and 931 (shaded circles) keV lines from the iron target. The data for the 847 keV line have been increased by a factor of 10.

lute cross sections to 17%. The relative cross sections are still accurate to 10%. These excitation functions are given in Table II.

SILICON TARGET

A thin silicon wafer 7.56 mg/cm^2 thick was bombarded and six lines between 780 and 1778 keV energy were extracted. The 780 keV line results from the decay of the second excited state to the ground state in ^{27}Si. The 959 line results from the decay of the first excited state to the ground state in ^{27}Si (956.8 keV) and from the sixth excited state to the third excited state in ^{29}Al (960.3 keV). The 844 and 1014 keV lines result from the decay of the second and the first excited states to the ground state in

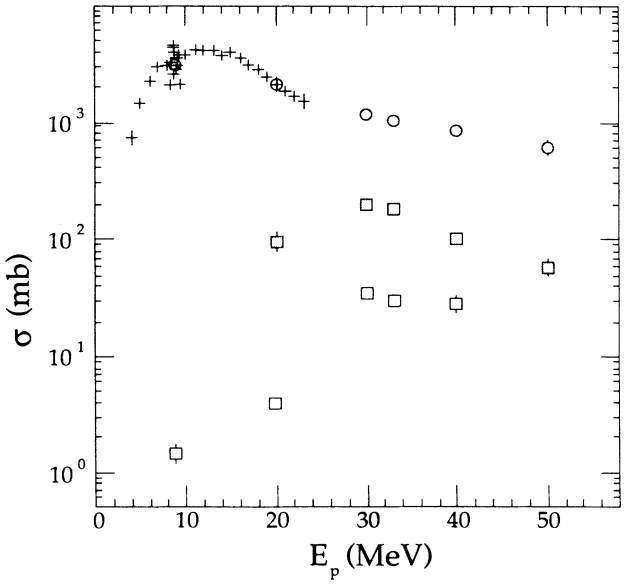

FIG. 12. γ-ray production cross sections for the production of the 1014 (open boxes), 1369 (shaded boxes), and 1778 (shaded circles) keV lines from the silicon target. The data for the 1369 (1778) keV line have been increased by a factor of 2 (10), respectively.

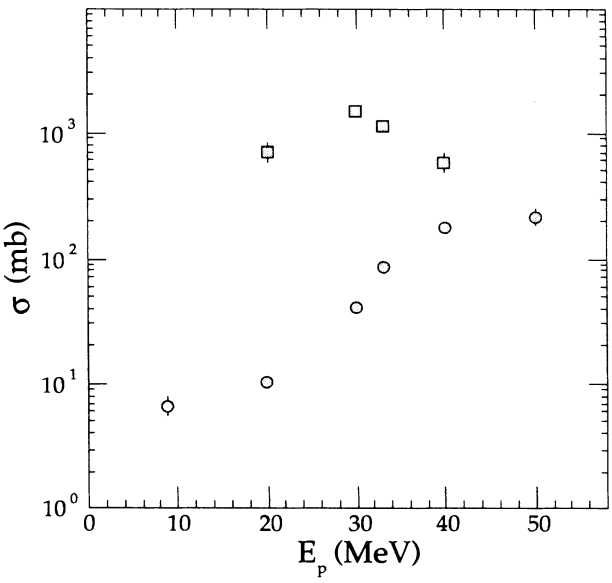

FIG. 14. γ-ray production cross sections for the production of the 1129 (shaded circles) and 1222 (shaded boxes) keV lines from the iron target. The data for the 1222 keV lines have been increased by a factor of 15.

^{27}Al. The 1369 keV line was produced in the decay of the first excited state of ^{24}Mg. The 1778 keV line was produced in the decay of the first excited state of ^{28}Si. The absolute cross sections for the 1778 keV line was renormalized to Ref. 7, the other lines were normalized by interpolating the absolute detection efficiency determined from other γ-ray lines and measured target thicknesses. The excitation functions are presented in Figs. 11 and 12.

IRON TARGET

A 2.1 mg/cm^2 foil of natural iron was used and eight lines were extracted from the spectra. The 847 and the 1238 keV lines result from the decay of the second to the first excited state and the first excited state to the ground state of ^{56}Fe. The 931 and the 1317 keV lines result from the decay of the third and the fourth excited states of ^{55}Fe to the ground state. The 1222 keV line result from the decay of the 12th to the third excited state of ^{55}Fe. The 1129 keV line is produced in the decay of second to the first excited state of ^{54}Fe. The 1408 keV line is a composite of two lines: the decay of the first excited state to the ground state of ^{54}Fe, and the decay of the fourth excited state to the ground state of ^{55}Fe. The 1435 keV line was composite of the decay of the third excited state to the ground state of ^{53}Mn and the first excited state to the ground state in ^{52}Cr. The 847, 931, 1238, and 1317 lines were normalized to Ref. 7. The absolute detection efficiency was obtained from these normalizations and used to normalize the other lines. The excitation functions are shown in Figs. 13–16.

DISCUSSION

In an earlier work, Ramaty *et al.*[3] used the differential cross sections of Foley *et al.*[14] and Zobel *et al.*[10] to deduce total, angle integrated γ-ray production cross sections. This procedure is risky because the measurements were made at a single angle and it is difficult to deduce accurate total cross sections without angular distribution data. When comparisons between our data and those summarized by Ramaty *et al.* can be made, we find that the two data sets agree at the 20–50% level. However, for many of the systems we find a much smaller energy dependence of the production cross sections, such that our cross sections at higher energies differ significantly from those of Ref. 10. Comparisons made between our measurements and those of Lang *et al.*[12] indicate a general agreement for most of the systems.

While the actual number of extra-terrestrial γ-ray sources remains limited to a few, and while the number of γ-ray lines which have been unambiguously identified is even fewer, it is hoped that with additional observations of γ-ray sources in the coming years the γ-ray production cross sections we present here will be of value in determining quantities such as the modes and sites of nucleosynthesis, particle fluxes, and nuclear abundances in the ISM.

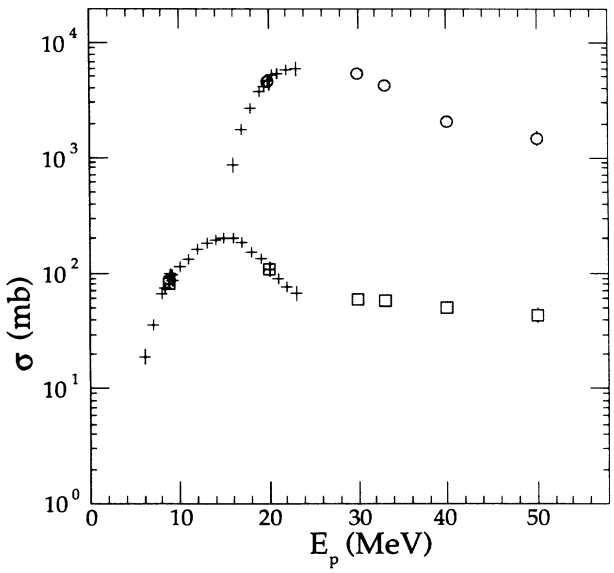

FIG. 15. γ-ray production cross sections for the production of the 1238 (shaded circles) and 1317 (shaded boxes) keV lines from the iron target. The data for the 1317 keV line data have been multipled by a factor of 30.

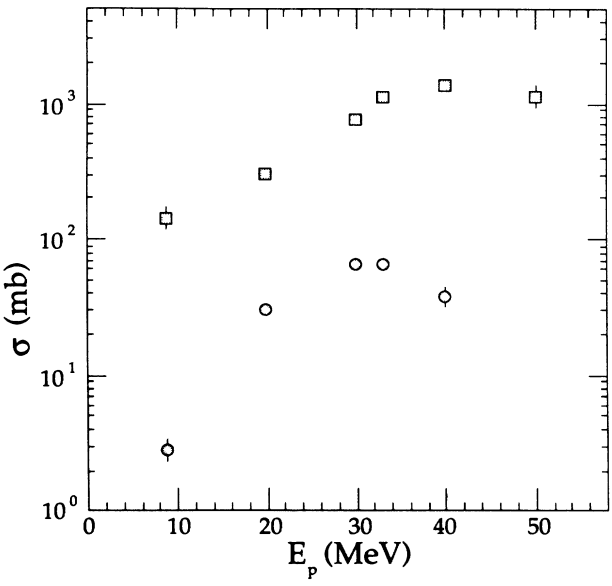

FIG. 16. γ-ray production cross sections for the production of the 1408 (shaded boxes) and 1435 (shaded circles) keV lines from the iron target. The data for the 1408 keV line data have been multiplied by a factor of 5.

ACKNOWLEDGMENTS

We would like to express our appreciation to E. Horsch for his assistance with some of the data analysis. One of us (D.M.M.) wishes to thank the Monticello Foundation for support during her visit to Lawrence Berkeley Laboratory (LBL). This work supported by the Director, Office of Energy Research, Division of Nuclear Physics of the Office of High Energy and Nuclear Physics of the U.S. Department of Energy under Contract No. DE-AC03-76SF00098.

*Present address: Physics Department, University of Washington, Seattle, WA 98195.
†Present address: Astronomy Department, Columbia University, New York City, NY 10027.
‡Present address: Molecular Design Ltd., San Leandro, CA 94577.

[1]E. L. Chupp, D. J. Forrest, P. R. Higbie, A. N. Suri, C. Tsai, and P. P. Dunphy, Nature **241**, 333 (1973).
[2]R. Ramaty and R. E. Lingenfelter, Annu. Rev. Nucl. Part. Sci. **32**, 235 (1982); NASA Technical Memorandum Report No. 79619 (unpublished).
[3]R. Ramaty, B. Kozlovsky, and R. E. Lingenfelter, Astrophys. J. Suppl. **40**, 487 (1979).
[4]R. C. Lamb, J. C. Ling, W. A. Mahoney, G. R. Riegler, W. A. Wheaton, and A. S. Jacobson, Nature **305**, 37 (1983); C. J. MacCallum, A. F. Huters, P. D. Stang, and M. Leventhal, Astrophys. J. **291**, 486 (1985); R. Ramaty, B. Kozlovsky, and R. E. Lingenfelter, Astrophys. Lett. **283**, L13 (1984); J. Shaham, Comments Astrophys. **9**(1), 1 (1980).
[5]M. Leventhal, J. C. MacCallum, and A. C. Watts, Astrophys. J. **216**, 491 (1977).
[6]R. E. Lingenfelter and R. Ramaty, Phys. Today **31**(3), 40 (1978).
[7]P. Dyer, D. Bodansky, A. G. Seamster, E. B. Norman, and D. R. Maxson, Phys. Rev. C **23**, 1865 (1981); and private communication.
[8]P. Dyer, D. Bodansky, D. D. Leach, E. B. Norman, and A. G. Seamster, Phys. Rev. C **32**, 1873 (1985).
[9]A. G. Seamster, E. B. Norman, D. D. Leach, P. Dyer, and D. Bodansky, Phys. Rev. C **29**, 394 (1984).
[10]W. Zobel, F. C. Maienschein, J. H. Todd, and G. T. Chapman, Nucl. Sci. Eng. **32**, 392 (1968).
[11]C. M. Lederer and V. S. Shirley, *Table of Isotopes*, 7th ed. (Wiley, New York, 1978).
[12]F. L. Lang, C. W. Werntz, C. J. Crannell, J. I. Trombka, and C. C. Chang, Phys. Rev. C **35**, 1214 (1987).
[13]J. Narayanaswamy, P. Dyer, S. R. Faber, and S. M. Austin, Phys. Rev. C **24**, 2727 (1981).
[14]K. J. Foley, A. B. Clegg, and G. L. Salmon, Nucl. Phys. **37**, 23 (1962).

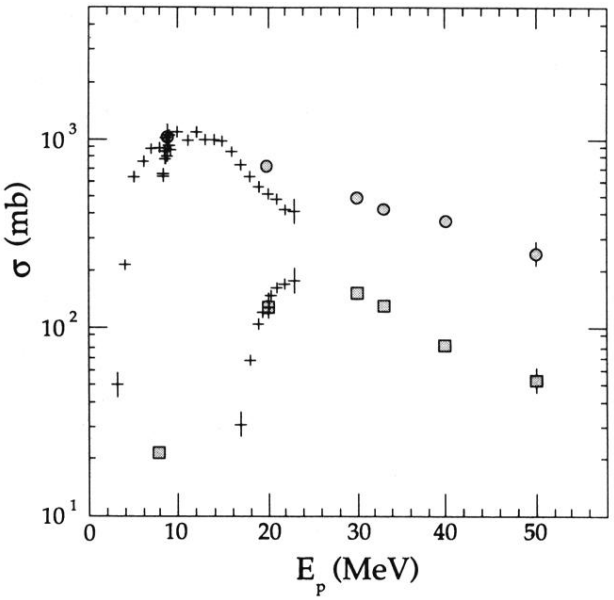

FIG. 10. γ-ray production cross sections for the production of the 1369 (shaded circles) and 1635 (shaded boxes) keV lines from the magnesium target. The data for the 1369 keV line have been increased by a factor of 2. The discrepancy between our data and those of Ref. 7 at 20 MeV for the 1369 keV line is explained by the additional isotopes in our target which contributed to the yield at 20 MeV, where as Dyer *et al.* used an isotopically enriched target.

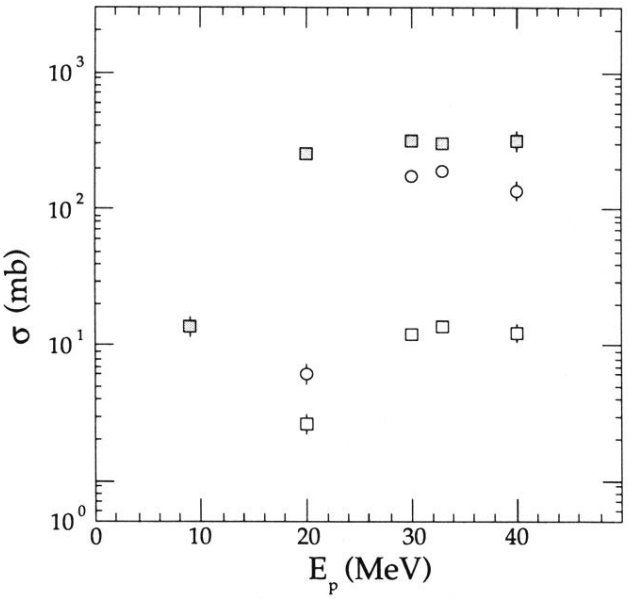

FIG. 11. γ-ray production cross sections for the production of the 780 (open boxes), 844 (shaded boxes), and 959 (open circles) keV lines from the silicon target. The data for the 844 (959) keV line have been increased by a factor of 15 (10), respectively.

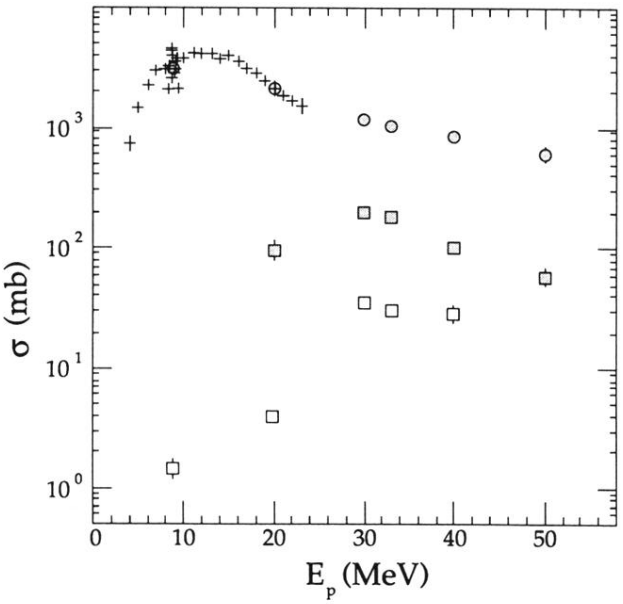

FIG. 12. γ-ray production cross sections for the production of the 1014 (open boxes), 1369 (shaded boxes), and 1778 (shaded circles) keV lines from the silicon target. The data for the 1369 (1778) keV line have been increased by a factor of 2 (10), respectively.

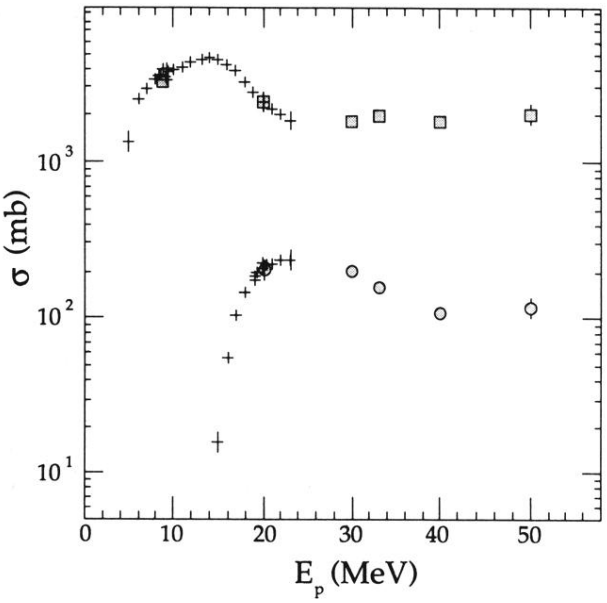

FIG. 13. γ-ray production cross sections for the production of the 847 (shaded boxes) and 931 (shaded circles) keV lines from the iron target. The data for the 847 keV line have been increased by a factor of 10.

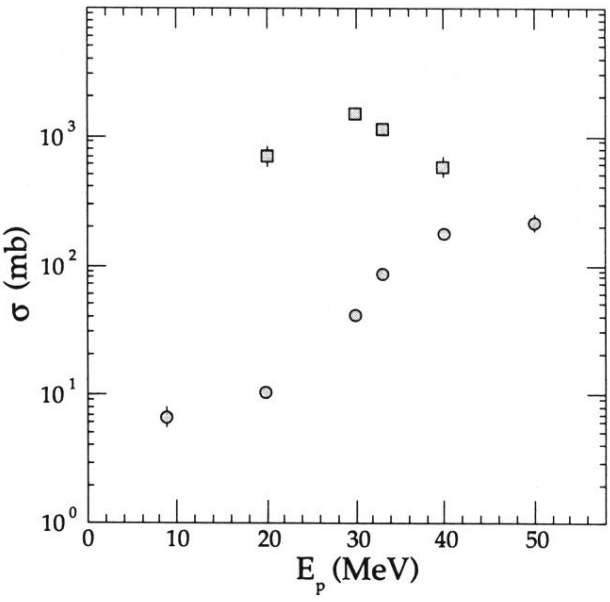

FIG. 14. γ-ray production cross sections for the production of the 1129 (shaded circles) and 1222 (shaded boxes) keV lines from the iron target. The data for the 1222 keV lines have been increased by a factor of 15.

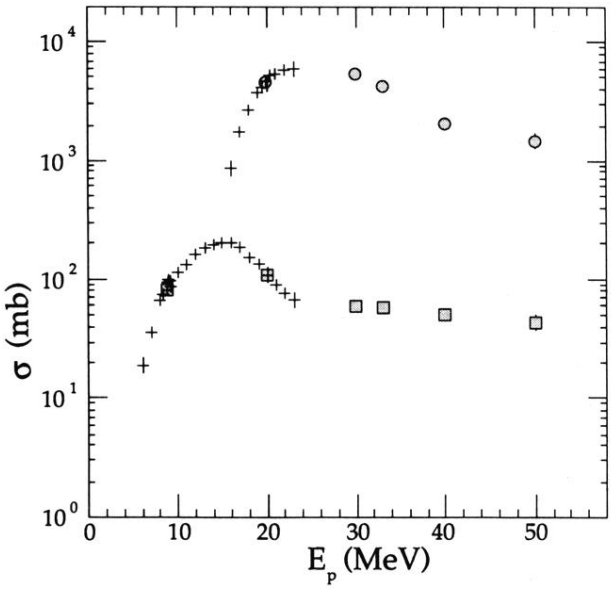

FIG. 15. γ-ray production cross sections for the production of the 1238 (shaded circles) and 1317 (shaded boxes) keV lines from the iron target. The data for the 1317 keV line data have been multipled by a factor of 30.

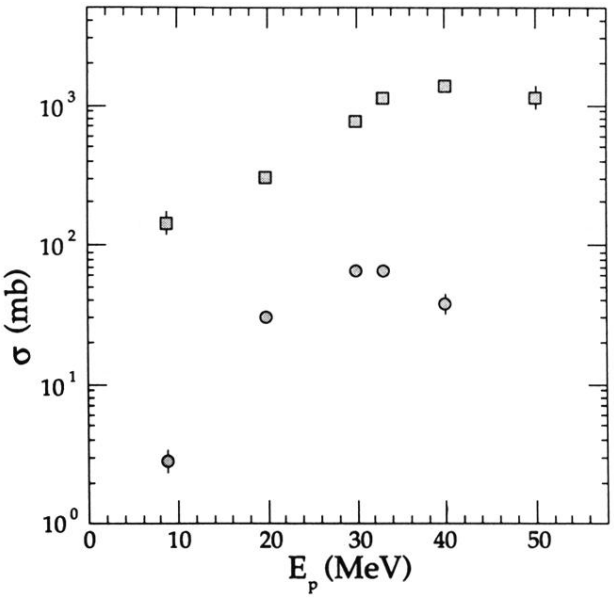

FIG. 16. γ-ray production cross sections for the production of the 1408 (shaded boxes) and 1435 (shaded circles) keV lines from the iron target. The data for the 1408 keV line data have been multiplied by a factor of 5.

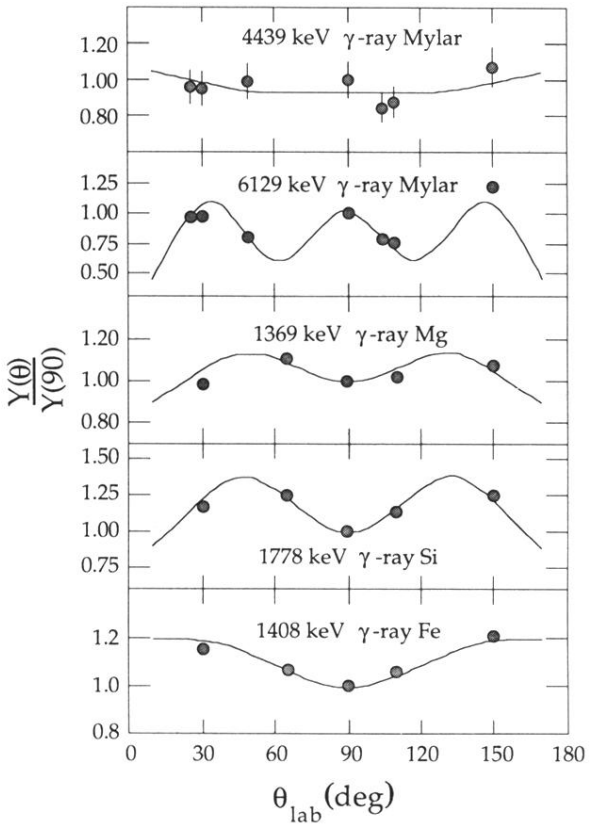

FIG. 5. Angular distributions for five separate γ-ray transitions resulting from the bombardment of Mylar, Mg, Si, and Fe targets with 33 MeV protons. The solid lines are the results of least squares fits of Legendre polynomials to the data.

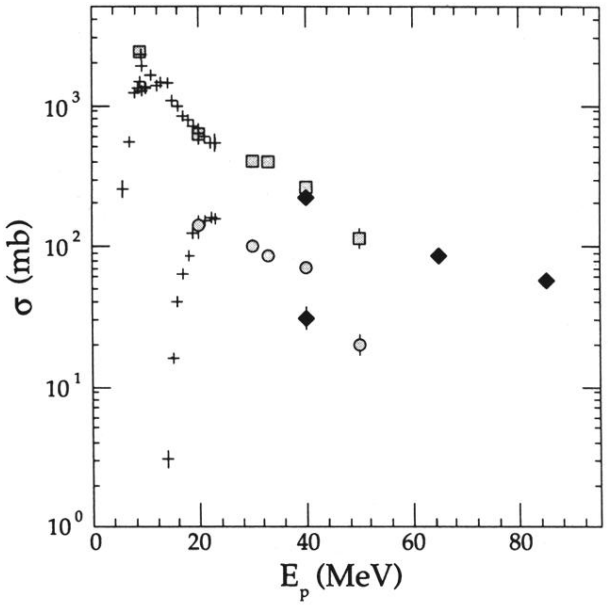

FIG. 6. γ-ray production cross sections for the production of the 4439 keV line from carbon and oxygen targets are indicated by the shaded boxes and shaded circles, respectively. In this and subsequent figures the data of Ref. 7 are plotted as small crosses and those of Ref. 12 are presented as solid diamonds. The data from the carbon target have been multiplied by a factor of 5. Representative errors are indicated on a number of data points for this and subsequent figures.

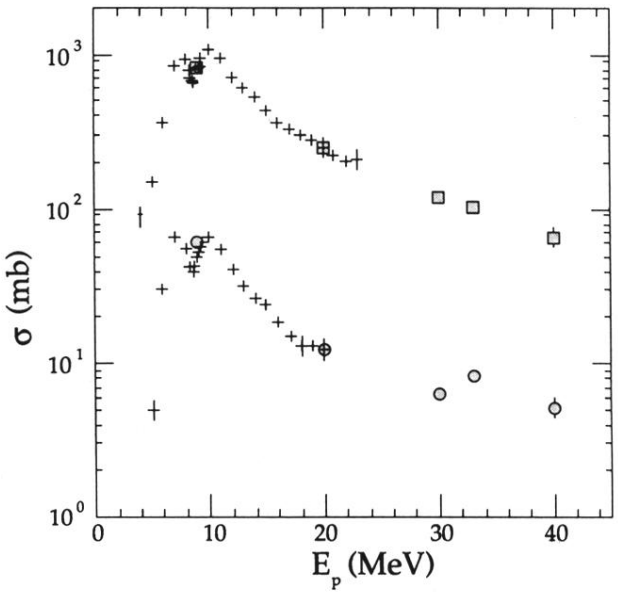

FIG. 7. γ-ray production cross sections for the production of 1635 (shaded circles) and 2315 (shaded boxes) keV lines from the nitrogen target. The data for the 2315 keV line have been multiplied by a factor of 10.

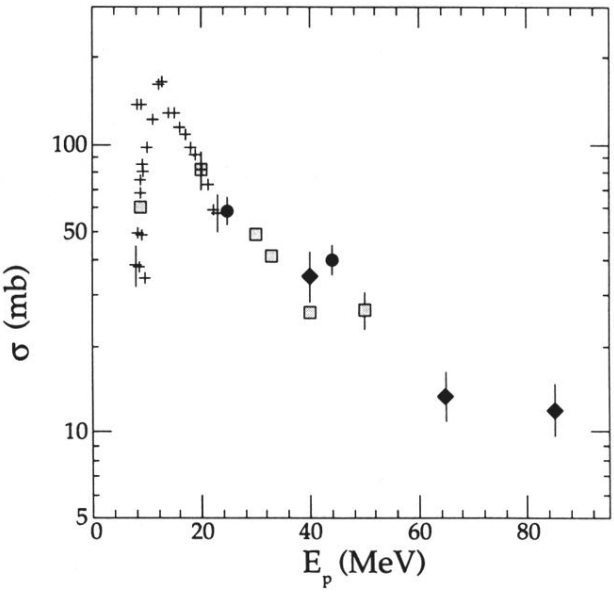

FIG. 8. γ-ray production cross sections for the production of the 6129 keV line from oxygen target (shaded boxes). In addition to the data of Refs. 7 and 12, those of Ref. 13 are shown with solid circles.

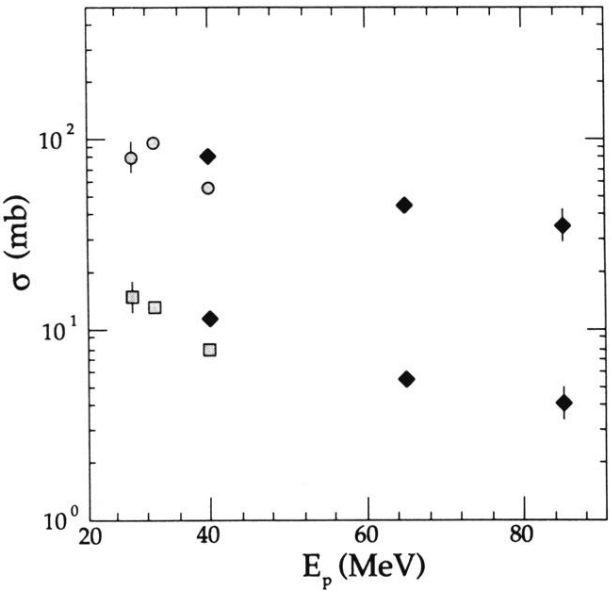

FIG. 9. γ-ray production cross sections for the production of the 5241 (shaded circles) and 5270 (shaded boxes) keV lines from the oxygen target. The data for the 5241 keV line have been increased by a factor of 5.